Extreme Mechanics Letters 49 (2021) 101483

Contents lists available at ScienceDirect

Extreme Mechanics Letters

journal homepage: www.elsevier.com/locate/eml

Geometric mechanics of folded kirigami structures with tunable bandgap

Yanbin Li [a,1], Xiaolei Song [b,1], Haijun Liu [b,*], Jie Yin [a,*]

[a] Department of Mechanical and Aerospace Engineering, North Carolina State University, Raleigh, NC 27695, USA
[b] Department of Mechanical Engineering, Temple University, Philadelphia, PA 19122, USA

ARTICLE INFO

Article history:
Received 22 June 2021
Received in revised form 25 August 2021
Accepted 3 September 2021
Available online 4 October 2021

Keywords:
Kirigami structures
Foldable hinges
Structural polarization
Stiffness singularity
Tunable phononic bandgap

ABSTRACT

We study the geometric mechanics and tunable band structures of a recently developed new class of folded kirigami structures through experiments, theoretical modeling, and numerical simulation. The folded kirigami structures with square and triangular cut patterns are constructed by replacing the point hinge in conventional kirigami sheets with a 3D folding hinge. We find that the folded design can effectively overcome the polarization constraint in the conventional kirigami sheets without folds. Specially, as the creases continue to fold from 0° to 180°, the folded design achieves a unique polarization switch, i.e., the structure expands first and then shrinks to be even smaller than that before folding. Geometric mechanics models are developed to predict how the geometry of the folding hinges determines both the shape changes and structural responses, including nominal strains, polarization switch, Poisson's ratio, folding rate, surface porosity, and structural stiffness. The models are validated through related experiments. We find that the observed polarization switch corresponds to both the peak nominal strains and stiffness singularity in the structures. Lastly, we numerically explore its shape change induced tunable phononic bandgap structures. We find that for special designs with polarization switch, it leads to symmetric bandgap structures changing with the folding angle. This work could find potential applications in designing kirigami metamaterials, shape-morphing materials, and phononic materials with tunable band structures.

1. Introduction

Shape plays an important role in determining the properties and functionalities of mechanical structures. This is especially true for a kirigami structure. It harnesses the ancient art of paper cutting techniques for achieving shape morphing [1–7]. A kirigami sheet can either expand laterally with largely enhanced stretchability via rigid rotation [8–11], or morph into special 2D/3D shapes via out-of-plane buckling deformation [12–15]. Such 2D and 3D shape changes in kirigami sheets yield exceptional properties such as ultra-stretchability [9,11,13,16,17], negative Poisson's ratio [8,11,18], and programmable material properties [10,19]. The kirigami structures have found broad applications in mechanical metamaterials [3,20–23], ultra-stretchable devices [9,24–27], soft robots [28–31], phononics [10,32], and energy absorption, harvesting, and saving [20,33–35].

Compared to the widely explored different cut patterns in kirigami structures and their demonstrated broad applications, the studies on the geometry of hinges (i.e., the cut tip) that connect the cut units receive limited attention. The hinges are also key to determining its shape-changing behavior and correlated properties [36]. In most kirigami designs, the hinges are thin and commonly simplified as a point joint. During shape shifting, the hinges often undergo severe stress concentration. Thus, the hinges are susceptible to failure to devastating its structural performances. To reduce their stress concentration, we proposed a strategy of redesigning the hinges' local shape to achieve enhanced stretching strength in kirigami sheets [10]. Recently, Rafsanjani and Bertoldi [14] have demonstrated the importance of hinges' width in determining the different shape-changing modes in a uni-axially stretched kirigami sheet. They found that for a kirigami sheet with the same cut pattern, when the hinge is relatively thinner, it favors in-plane deformation through rigid rotation, while for relatively wider hinges, it prefers to buckle out of plane to form 3D pop-up structures. Very recently, we have proposed redesigning the unstructured hinges with a foldable 3D hinge to release the constrained degrees of freedom in both deformation and actuation [29]. Through controllable self-folding in the hinges, we achieved the remote actuation of both 2D and 3D shape shifting in kirigami sheets in response environmental temperature. The folds in the hinges could add new dimensions and largely expand the potential design space

* Corresponding authors.
E-mail addresses: haijun@temple.edu (H. Liu), jyin8@ncsu.edu (J. Yin).
[1] These authors contributed equally to this work.

https://doi.org/10.1016/j.eml.2021.101483
2352-4316/

in conventional kirigami sheets with sole cuts. However, it remains largely unexplored in previous studies [10,14,29], concerning how to quantify the effects of added folds on the shape changes, as well as shape-determined mechanical and phononic responses in kirigami sheets.

Following our previous work [29], in this paper, we systematically exploit how the geometry of foldable hinges affect the deformation and mechanical behavior of the folded kirigami structures through geometric mechanics models. The folded kirigami structures are constructed by replacing the point hinge in the conventional kirigami sheet with a 3D folding hinge that is composed of three mountain and valley creases. The introduced folding adds several new geometrical and shape-changing parameters such as the cut length, the angle between the mountain and valley creases, and the folding angles in the creases. Through the geometric mechanics model, we explore quantifying the effects of these new parameters on the shape changes and structural responses in terms of nominal strains, folding rates, surface porosity, and structural stiffness. We find that the folded kirigami structure shows a tunable maximum opening angle by the inclined angle of valley creases, as opposed to a constant value in the conventional kirigami sheet. Thus, it enables the unique shape changes of folding-induced opening and reclosing of the cuts. Enhanced by the folding hinges, it achieves a larger tunable design space of nominal strains, structural porosity, and structural stiffness than the conventional kirigami designs. We further explore its shape changing induced tunable phononic band structures of the folded kirigami structures. We find that it shows a larger bandwidth tunability than the conventional kirigami design.

This paper is organized as follows. Section 2 describes the design details and shape-changing features of the two example folded kirigami structures in a square and triangular cut pattern. Section 3 discusses the developed geometric mechanics models to quantify the effects of introduced folds on their geometrical shape and structural stiffness changes, as well as model validation through experiments. Section 4 discusses the numerical simulation results on the tunable band structures of the folded kirigami structures via folding-induced shape changes. Finally, Section 5 concludes this work.

2. Shape change of the folded kirigami structures

Fig. 1 displays the construction of two example folded kirigami structures with the classical square (Fig. 1A and B) and triangular cut patterns (Fig. 1C and D), as well as their shape changes in both a single unit and a periodic tessellated form. We replace the point-joint hinges in conventional kirigami sheets [11] using a spatial folding hinge. As shown in the left column of Fig. 1, the hinge consists of three line folds: one mountain crease and two symmetric valley creases. The physical prototypes are fabricated using thin sheets of copy paper with prescribed cutting and engraved creasing patterns via a laser cutter. To reduce the stress concentration and avoid material failure during folding, circular-shaped cutouts (see the zoomed-in highlights in Fig. 1A(ii)) are introduced at each cut tip.

Upon stretching, the three creases start to fold around the line hinges. Consequently, the two triangular facets hinged by the mountain crease pop up, forming a tetrahedron hinge in both square and triangular-cut sheets (2nd column of Fig. 1). Meanwhile, the connected cut units rotate rigidly in plane around the creases to open the initially line cuts or slits and form a pore (highlighted in yellow color). Similar to their non-folded counterparts with point-joint hinges [11], the two folded kirigami structures exhibit single degree of freedom deformation and expand in both lateral directions via hinge folding. The pore is initially polarized along the vertical direction (2nd column of Fig. 1) until it is maximally opened (3rd column of Fig. 1). The maximally opened configuration defines a critical state of polarization switch. Beyond it, the polarized direction of the pores will be switched to the horizontal axis upon further folding. Then, the structure starts to contract until the two triangular facets meet and contact with each other (4th column of Fig. 1). It should be noted that the polarization switch is not observed in its counterpart with point-joint hinges due to its infinite stiffness at the critical state [11].

3. Geometric mechanics of the folded kirigami structures

To better understand the observed polarization switch, in this section, we exploit how the geometry of the folds affects the shape change (Sections 3.1 and 3.2) and mechanical behavior (Section 3.3) in the folded kirigami structures through both geometry and mechanics models. Here we assume that all the triangular facets and the cut units are rigid and the line folds are modeled as linearly elastic torsional springs.

3.1. Folded kirigami structures with square cuts

3.1.1. Folding angle relationship and folding rate

Fig. 2A shows the schematic shape changes in the folded kirigami structures with square cuts. The geometry of the square cut unit cell can be characterized by the side length a_0, the cutting ratio m_s that is defined as the ratio of length of cuts d to the unit cell length a_0 (i.e., $0 < m_s{=}d/a_0 < 1$ with the subscript "s" denoting the case of square cuts), and the inclined angle φ_0 defined as the angle between the mountain crease and the symmetric valley creases (Fig. 2A, bottom). As m_s varies from 0 to 1, it corresponds to an increasing cut length or equivalently a decreasing hinge width (i.e., $a_0 - d$). Compared to the conventional kirigami sheet without folds (i.e., the extreme case of $m_s = 1$ with $d = a_0$) [11], the folded kirigami design adds a new dimension of an inclined angle φ_0. After folding, the deformed shape can be parametrized by the deformed length a of the unit cell, the opening angle η_s between cuts with $\eta_s \in [0, 2\varphi_0]$ (Fig. 2B, bottom left), as well as the folding angles at the mountain crease $\gamma_m \in [0, \pi]$ and valley crease $\gamma_v \in [0, \pi/2]$ in the tetrahedron hinge $KK_1K_2K_3$ (Fig. 2B, bottom right). When the mountain creases become fully folded, i.e., $\gamma_m = \pi$, we will have $\gamma_v = \pi/2$ and $\eta_s = 2\varphi_0$ (Fig. 2C, bottom) as discussed in the following.

We note that the opening angle and the folding angles are geometrically dependent of each other. From the tetrahedron hinge in the bottom right of Fig. 2B, we can obtain the following geometrical relations, i.e., $KO_1 \perp K_1K_2$, $KO_2 \perp K_2K_3$, $K_3O_1 \perp K_1K_2$, $KK_1 \perp KK_3$, $KK_2 \perp KK_3$, $K_1K_3 = K_2K_3$ and $KO_1 \perp S_{K_1K_2K_3}$, where $S_{K_1K_2K_3}$ is the bottom surface of the tetrahedron hinge. Then, we can readily derive the folding angles of both mountain and valley creases as

$$\gamma_m = \pi - 2\arcsin\left(\frac{\sin(\varphi_0 - \eta_s/2)}{\sin\varphi_0}\right) \tag{1}$$

$$\gamma_v = \arcsin\frac{\cos(\gamma_m/2)}{\sqrt{\sin^2\varphi_0\cos^2(\gamma_m/2) + \cos^2\varphi_0}} \tag{2}$$

Eqs. (1) and (2) show that the deformation of the folded kirigami structures can be characterized by the single degree of freedom opening angle η_s or equivalently the mountain folding angle γ_m. Both the opening angle and the folding angles are dependent of the inclined angle φ_0. Fig. 3A(i) shows the variations of η_s as a function of γ_m and γ_v as φ_0 increases from $\pi/6$ to $5\pi/12$. It shows that η_s increases monotonically with both γ_m and γ_v. As the creases start to fold, the line cuts are open. The opening angle η_s increases with the folding angle γ_m. At the completely folded

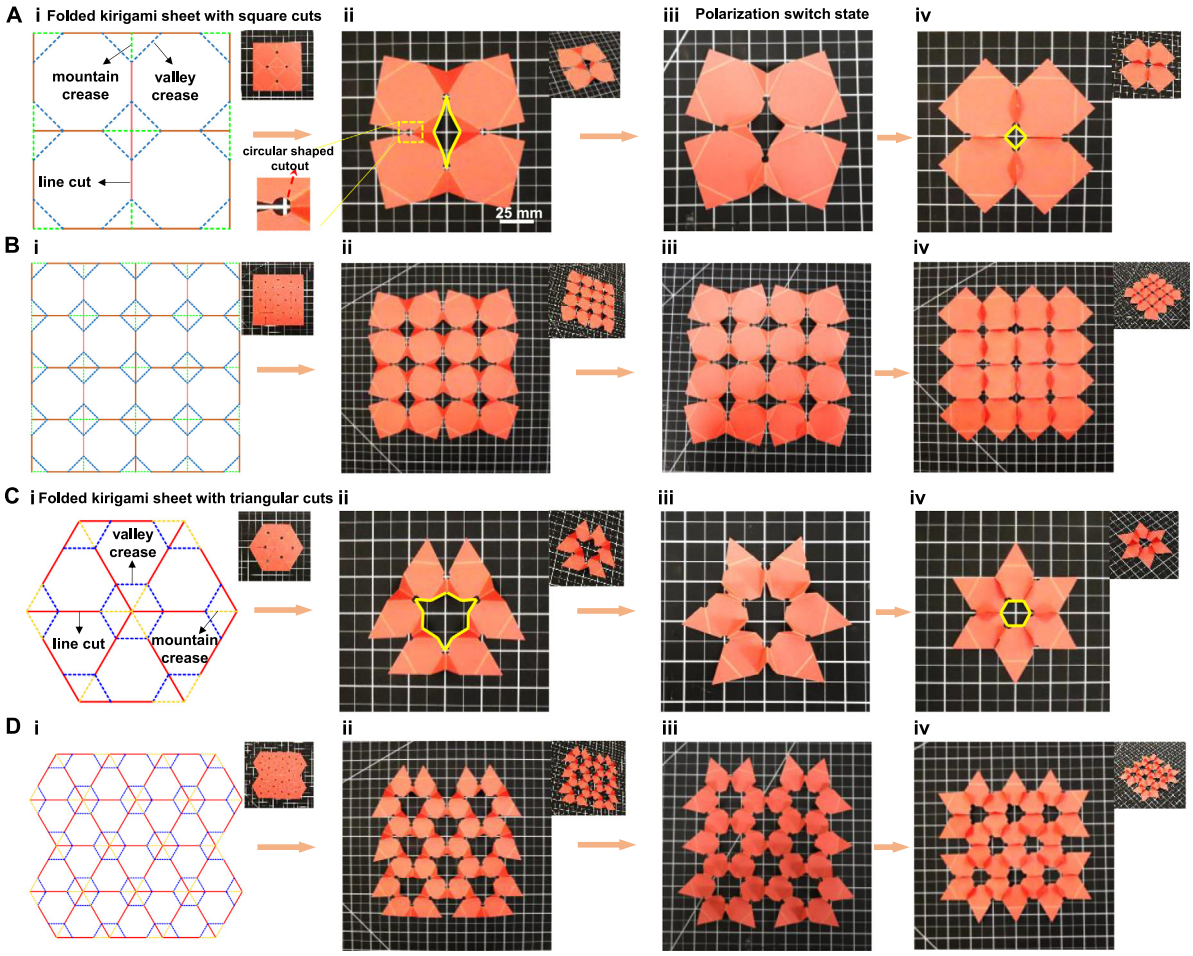

Fig. 1. Design of shape-changing folded kirigami structures with foldable hinges. (A, B) Shape changes of paper-based folded kirigami structures with square cuts via folding in the hinges in the form of a single unit (A) and periodic units (B). (C, D) Shape changes in folded kirigami structures with triangular cuts. Column (i) show the schematic design by introducing three intersecting creases composed of one mountain crease and two symmetric valley creases to the tip of line cut to form a foldable tetrahedron hinge. Column (ii-iv) show the shape changes during the folding of the creases. The polarized direction is switched from vertical in column (ii) (i.e., the diagonal of the highlighted pore) to horizontal in column (iv) (completely folded state). The intermediate deformed shapes in column (iii) defines the critical polarization switch state.. (For interpretation of the references to color in this figure legend, the reader is referred to the web version of this article.)

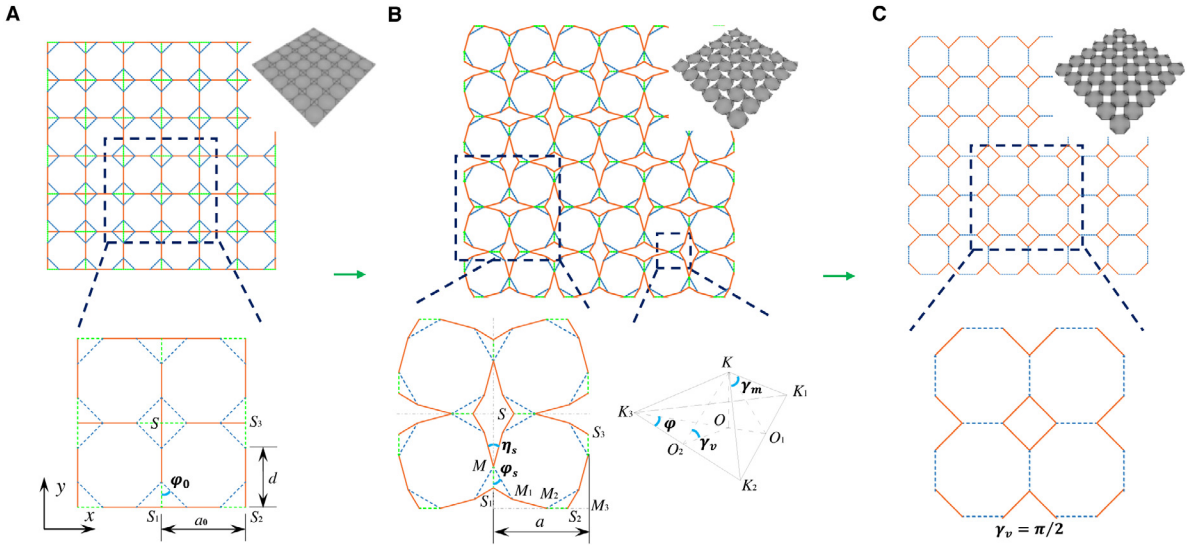

Fig. 2. Schematic of the projected view of shape changes in folded kirigami structures with square cuts. (A) non-folded state, (B) partially folded state, (C) completely folded state with the valley folding angle $\gamma_v = \pi/2$. Bottom row shows the schematics of the geometrical parameters in each folded state.

state, i.e., $\gamma_m = \pi$ or $\gamma_v = \pi/2$, η_s reaches its maximum value, i.e., the maximum opening angle $(\eta_s)_{\max}$. Setting $\gamma_m = \pi$ in Eq. (1)

gives

$$(\eta_s)_{\max} = 2\varphi_0 \tag{3}$$

Thus, different φ_0 ends with different maximum η_s shown in Fig. 3A. Eq. (3) indicates that the maximum opening angle in a folded kirigami structure can be tuned by the inclined angle φ_0 of the creases. This is in contrast to the constant value of $(\eta_s)_{\max} = \pi/2$ in its non-folded counterparts with point joints [14]. Thus, higher $(\eta_s)_{\max}$ than $\pi/2$ can be readily achieved in the folded kirigami structures by setting $\varphi_0 \geq \pi/4$. For example, for the case with $\varphi_0 = 5\pi/12$, both γ_m-η_s and γ_v-η_s curves end at $(\eta_s)_{\max} = 5\pi/6 = 2\varphi_0$, which is close to π when it becomes completely folded. This is consistent with the experimental observation in the corresponding physical prototype of paper kirigami structures shown in Fig. 3B(i).

To characterize the surface morphology of the folded kirigami structures induced by the out-of-plane folding of the tetrahedron hinges, we define the folding rate k_s as

$$k_s = \tan\gamma_v = \tan\left\{\arcsin\frac{\cos(\gamma_m/2)}{\sqrt{\sin^2\varphi_0\cos^2(\gamma_m/2)+\cos^2\varphi_0}}\right\} \tag{4}$$

Geometrically, k_s represents the slope of side triangular facet $S_{KK_2K_3}$ or $S_{KK_1K_3}$ (Fig. 2B, bottom-right) in the tetrahedron hinge. Based on Eqs. (1)–(4), Fig. 3A(ii) shows the change of k_s for the folded kirigami structures with different φ_0 during the pore opening. It shows that a larger inclined angle leads to a higher folding rate. Overall, the folding rate k_s for all the cases shows a *J*-shaped trend, which increases dramatically when it approaches to its respective maximum opening angle $(\eta_s)_{\max} = 2\varphi_0$ in Eq. (3).

3.1.2. Nominal strain and surface porosity

Nominal strain: Based on Eqs. (1)–(2), the nominal strain $(\varepsilon_{xx})_s$ along the *x*-axis can be expressed as $(\varepsilon_{xx})_s = (a - a_0)/a_0$. From Fig. 2B (bottom left), we have

$$a = MM_1\sin\varphi_s + M_1M_2\cos\eta_s + MM_1\cos\varphi_s + M_1M_2\sin\eta_s \tag{5}$$

where MM_1 is the length of the valley crease, M_1M_2 is part of the cutting line, and φ_s is the projected angle between the valley creases and the mountain crease after folding. Substituting $MM_1 = (a_0 - d)/\cos\varphi_0$ and $M_1M_2 = d - (a_0 - d)\tan\varphi_0$ into Eq. (5), it gives

$$a = \sqrt{2}\left\{\frac{(a_0-d)}{\cos\varphi_0}\left(\sin\left(\frac{\pi}{4}+\varphi_0-\frac{\eta_s}{2}\right)\right) + [d-(a_0-d)\tan\varphi_0]\sin\left(\frac{\pi}{4}+\frac{\eta_s}{2}\right)\right\} \tag{6}$$

where the condition $M_1M_2 = d - (a\text{–}d)\tan\varphi_0 > 0$ must be satisfied. It implies that $\tan\varphi_0 \leq d/(a\text{-}d) = m_s/(1-m_s)$, i.e.,

$$0 < \varphi_0 \leq \arctan\left(\frac{m_s}{1-m_s}\right) \tag{7}$$

Eq. (7) imposes a geometrical constraint on the maximum inclined angle $(\varphi_0)_{\max}$ that could be prescribed in the creases for a given cutting ratio m_s, i.e., $(\varphi_0)_{\max} = \arctan[m_s/(1-m_s)]$ with $0 < m_s < 1$. Thus, for a folded kirigami structure with cutting ratio m_s, based on Eqs. (3) and (7), in principle, it can achieve a limit of the maximum opening angle $(\eta_s)_l$

$$(\eta_s)_l = 2(\varphi_0)_{\max} = 2\arctan\left(\frac{m_s}{1-m_s}\right) \tag{8}$$

at $(\varphi_0)_{\max} = \tan^{-1}[m_s/(1-m_s)]$.

Considering the structural symmetry, from Eq. (6), the nominal strains $(\varepsilon_{xx})_s$ and $(\varepsilon_{yy})_s$ of the folded square-cut kirigami structure along both *x*- and *y*-axis can be derived as

$$(\varepsilon_{xx})_s = (\varepsilon_{yy})_s = \frac{a-a_0}{a_0} = \sqrt{2}\left\{\frac{(1-m_s)}{\cos\varphi_0}\left(\sin\left(\frac{\pi}{4}+\varphi_0-\frac{\eta_s}{2}\right)\right) + [m_s-(1-m_s)\tan\varphi_0]\sin\left(\frac{\pi}{4}+\frac{\eta_s}{2}\right)\right\} - 1 \tag{9}$$

Eq. (9) characterizes the analytical correlation between the nominal strains and the opening angle or equivalently the mountain folding angle via Eq. (1) during the shape change. It also shows that the strains are dependent of the prescribed geometrical parameters such as the inclined angle φ_0 and the cutting ratio m_s.

We first explore the effect of φ_0 on ε_{xx} for the folded kirigami structures with fixed $m_s = 0.8$ by plotting the ε_{xx} *vs.* γ_m curves in Fig. 3A(iii). As γ_m increases from 0 to π, it shows that ε_{xx} increases monotonically for the case with a smaller φ_0 (e.g., $\varphi_0 = \pi/12$ and $\pi/6$), indicating that the structure always expands as it becomes completely folded. However, for the case with φ_0 larger than $\pi/4$, ε_{xx} increases first (expanding) and then decreases (shrinking) with the increase of γ_m, showing a peak strain $(\varepsilon_{xx})_{s\text{-max}}$. Thus, for folded kirigami structures with a given m_s, there exists a critical value of $(\varphi_0)_c$, beyond which the polarization switch occurs, i.e., $\varphi_0 \geq (\varphi_0)_c$. We note that the structures with different values of φ_0 show the same value of $(\varepsilon_{xx})_{s\text{-max}} = 0.166$ (the horizontal dash line in Fig. 3A(iii)) for $m_s = 0.8$, indicating that $(\varepsilon_{xx})_{s\text{-}max}$ is independent of φ_0. As shown in Fig. 3A(iii), as φ_0 increases, the nominal strain at the completely folded state (i.e., $\gamma_m = \pi$) decreases from a positive to even a negative value. This is consistent with the observed shape changes in both prototypes with different $\varphi_0 = 0.3\pi$ (Fig. 3B) and $\varphi_0 = 5\pi/12$ (Fig. 3C). Both prototypes have the same $m_s = 0.8$ and the same unfolded size highlighted by the yellow colored dashed square. Monotonic folding in the hinges leads to similar structural expansion-to-shrinkage transitions in both prototypes. At the completely folded state, compared to the size before folding (i.e., the yellow-colored dashed square), a slightly expanded shape is observed for $\varphi_0 = 0.3\pi$ (Fig. 3B(iv)), which corresponds to the small positive nominal strain in Fig. 3A(iii). However, for $\varphi_0 = 5\pi/12$, it shrinks to an even smaller size with nearly closed pores as shown in right of Fig. 3C, which corresponds to the negative nominal strain in Fig. 3A(iii).

We further plot ε_{xx} from Eq. (9) as a function of the opening angle η_s with constant $m_s = 0.8$ for the designs with different values of $\varphi_0 = \pi/6$, $\pi/3$, and $5\pi/12$ in Fig. 3A(iv). We find that all the curves for different φ_0 collapse into one overlapped curve, whereas η_s for each curve varies from 0 to $(\eta_s)_{\max} = 2\varphi_0$ for a given φ_0 based on Eq. (3). Thus, each curve ends with a different maximum opening angle. The corresponding experimental data agrees well with the model. From the unified curve for different φ_0, it shows that the peak strain $(\varepsilon_{xx})_{s\text{-max}}$ is achieved at the critical opening angle $(\eta_s)_c = 0.34\pi$, which also indicates that the corresponding critical inclined angle $(\varphi_0)_c$ for polarization switch is $(\varphi_0)_c = (\eta_s)_c/2 = 0.17\pi$ for $m_s = 0.8$. This is consistent with the observed polarization switch in the two prototypes, which have the same $m_s = 0.8$ but larger $\varphi_0 = \pi/3$ and $5\pi/12$ than $(\varphi_0)_c = 0.17\pi$ shown in Fig. 3B-C. We find that when beyond the critical opening angle $(\eta_s)_c = 0.34\pi$, the original polarized direction is switched from horizontal to vertical axis for $\varphi_0 = \pi/3$ shown in the transition from Fig. 3B(ii) to B(iii), and from vertical to horizontal for $\varphi_0 = 5\pi/12$ shown in Fig. 3C. Here, the polarized direction is defined as the orientation of the rhombus pore (highlighted in yellow color) along the long diagonal axis. Thus, for folded kirigami sheets with a given m_s, $(\varphi_0)_c$ could be identified by solving the corresponding $(\eta_s)_c$ to the peak strain

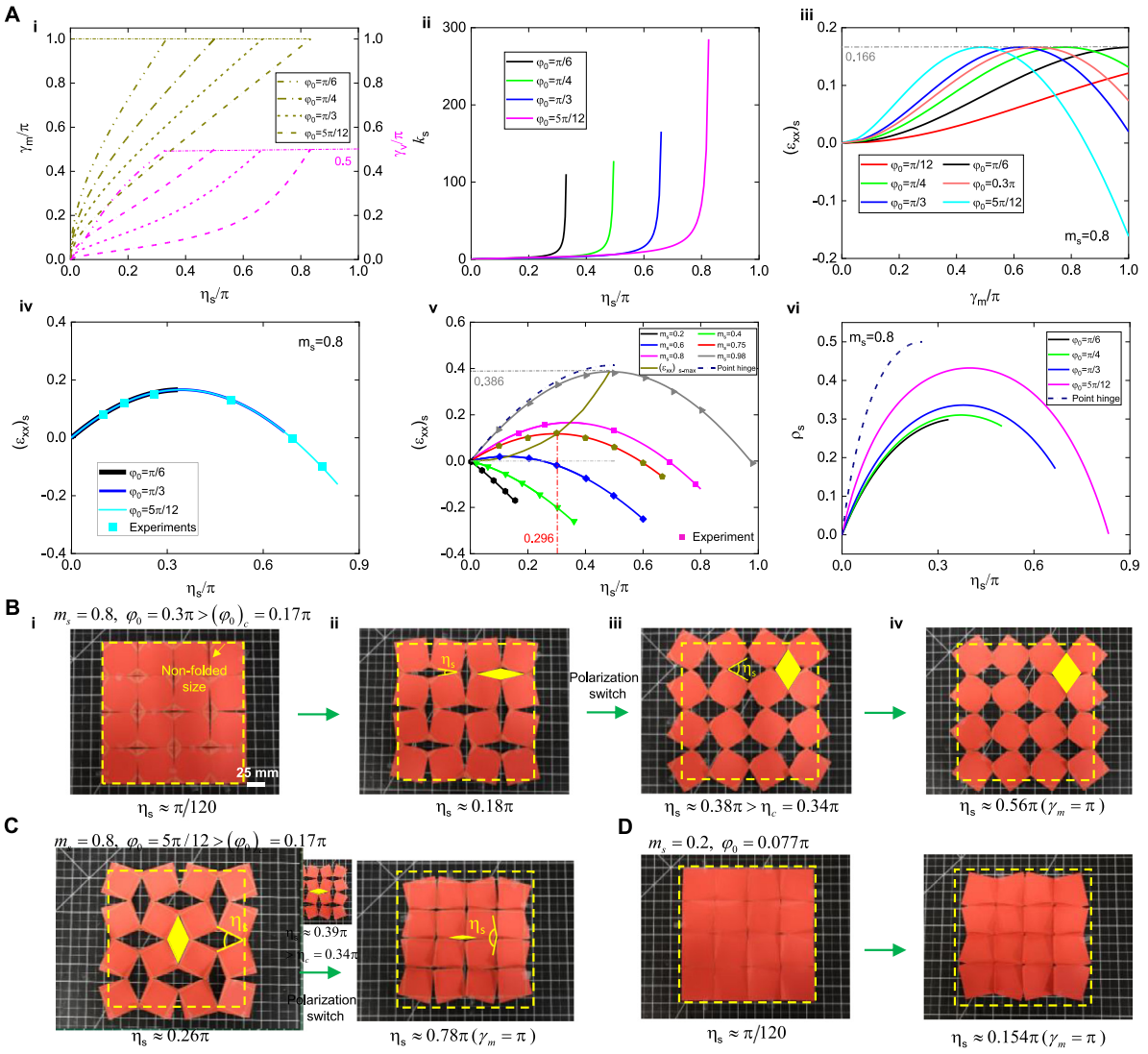

Fig. 3. Geometrical modeling of folded kirigami structures with square cuts. (A) (i): theoretical curves of mountain angle γ_m and valley angle γ_v vs. the opening angle η_s for designs with different inclined angles φ_0; (ii): theoretical curves of folding rate k_s vs. η_s for different φ_0; (iii): theoretical curves of nominal strain $(\varepsilon_{xx})_s$ vs. γ_m for different φ_0 at a fixed cutting ratio $m_s = 0.8$; (iv): theoretical curves of $(\varepsilon_{xx})_s$ vs. η_s for different φ_0 at $m_s = 0.8$. Symbols represent the corresponding measured experimental data points; (v): theoretical curves of $(\varepsilon_{xx})_s$ vs. η_s for different m_s. Symbols represent the corresponding measured experimental data points; (vi): theoretical curves of surface porosity ρ_s vs. η_s for different φ_0 at fixed $m_s = 0.8$. The dashed line in both (v) and (vi) represents the case of kirigami sheets with point hinge when m_t approaches to 1. (B-D) Demonstrated shape changes in three paper-based folded krigiami structure prototypes at representative values of η_s with $m_s = 0.8$, $\varphi_0 = 0.3\pi$ in (B) and $m_s = 0.8$, $\varphi_0 = 5\pi/12$ in (C), and $m_s = 0.2$, $\varphi_0 = 0.077\pi$ in (D). The three prototypes have the same size at the un-folded state highlighted by the yellow colored dashed square. (B) and (D) undergo polarization switch highlighted by the solid yellow color rhombus with its long diagonal axis rotated 90°.. (For interpretation of the references to color in this figure legend, the reader is referred to the web version of this article.)

$(\varepsilon_{xx})_{s\text{-max}}$ with $(\varphi_0)_c = (\eta_s)_c/2$ from Eq. (9), i.e., solving the function $f\left((\varphi_0)_c\right) = 0$ in the form of

$$f(\varphi_0)\big|_{\varphi_0=(\varphi_0)_c} = \frac{(\cos\varphi_0 - \sin\varphi_0)(1-m_s)\cos^2\varphi_0 - (m_s - (1-m_s)\sin\varphi_0)}{(\cos\varphi_0 + \sin\varphi_0)(1-m_s)\cos^2\varphi_0 + (m_s - (1-m_s)\sin\varphi_0)} - \tan\varphi_0 \tag{10}$$

Next, we explore the effect of the cutting ratio m_s on the variation of ε_{xx} for the folded kirigami structures by plotting the ε_{xx} *vs* η_s curves in Fig. 3A(v). Based on Eq. (8), we have $0 < \eta_s \leq (\eta_s)_l = 2(\varphi_0)_{max} = 2\arctan[m_s/(1-m_s)]$ for each curve with a given m_s. Similarly, each curve represents the collapsed curves for different values of φ_0 with $\varphi_0 \leq \arctan[m_s/(1-m_s)]$. For folded kirigami structures with a smaller m_s ($m_s \leq 0.4$), i.e., shorter line cuts, it shows a smaller maximum opening angle and a negative nominal strain that decreases monotonically with the increasing opening angle, meaning that the structure keeps shrinking as it becomes completely folded. This is consistent with the observed continuing shrinking size in the folded paper kirigami structure with $m_s = 0.2$ and $\varphi_0 = 0.077\pi$ shown in Fig. 3D. As m_s increases (e.g., $m_s \geq 0.6$), all the curves show a positive peak strain at $(\eta_s)_c$ for $(\varphi_0) \geq (\varphi_0)_c$, where the structure expands first with a positive nominal strain and then shrinks. Meanwhile, as m_s increases from 0.4 to 0.98, the nominal strain at the completely folded state increases from about −0.3 to 0. For different values of m_s, the measured nominal strains from experiments agree well with the geometric model as shown in Fig. 3A(v). Furthermore, we plot the curve of $(\varepsilon_{xx})_{s\text{-max}}$ *vs.* η_s as a function of m_s in Fig. 3A(v), which shows that the peak strain increases nonlinearly with m_s. By setting $m_s = 1$ in Eq. (9), it reduces to the case of conventional non-folded kirigami sheets with point joint hinges [11], where $(\varepsilon_{xx})_{s-\text{point-hinge}} = (\varepsilon_{yy})_{s-\text{point-hinge}} = \sqrt{2}\sin(\eta_s + \pi/4) - 1$. The

nominal strain increases monotonically with η_s and shows a maximum value of 0.414. Eq. (9) also presents a constant Poisson's ratio $v_s = -1$ for the folded kirigami sheets, which is the same as its counterpart without folds [11].

Surface Porosity: Given the characteristics of pore opening during deformation, we use the surface porosity ρ_s to characterize the overall pore area coverage of the folded kirigami structures. ρ_s is defined as the ratio of the projected area of the pores S_1 to the total area S, i.e.,

$$\rho_s = S_1/S \tag{11}$$

For the folded kirigami structures with square cuts, from Fig. 2B, we have $S_1 = a^2 - 4\,|OO_2|\,|K_2K_3|/2 - \left[a_0^2 - 4\,(a_0-d)^2\tan\varphi_0/2\right]$ and $S = a^2$, where $OO_2 = K_3O_2\tan\varphi_s = KK_3\cos\varphi_s\tan\varphi_s = (a_0-d)\cos\varphi_s\tan\varphi_s$, $K_3K_2 = (a_0-d)/\cos\varphi_s$. Thus, it gives

$$\rho_s = 1 - \frac{a_0^2}{a^2} + 2\left[(a_0-d)/a\right]^2(\tan\varphi_0 - \tan\varphi_s) \tag{12}$$

Combining Eqs. (6) and (12), Fig. 3A(vi) shows the change of ρ_s for folded kirigami structures with different inclined angle φ_0 during the pore opening at $m_s = 0.8$. ρ_s shows a peak value $(\rho_s)_{\max}$ with the increase of η_s for $\varphi_0 \geq \pi/6$ and $(\rho_s)_{\max}$ increases with φ_0. In addition, ρ_s increases with the increasing φ_0 at given η_s, whereas the porosity in the completely folded state decreases with the increasing φ_0. Notably, for the structure with a larger $\varphi_0 = 5\pi/12$, as γ_m increases from 0 to π, the porosity ρ_s varies from 0 (an initially closed pore) to a peak value of 0.432 (maximally opened pore), and then decreases to 0 again (pore re-closing), which is consistent with the experimental observation shown in Fig. 3B(i). We note that the peak porosity in the folded kirigami structures is slightly lower than the case of non-folded kirigami structures with point hinges ($(\rho_s)_{\max} = 0.5$ shown in Fig. 3A(vi)).

3.2. Folded kirigami structures with triangular cuts

Compared to the square cuts, the folded kirigami structure with triangular cuts is more complex due to its increased number of cuts and hinges. For the case of triangular cuts, given its special three-fold structural symmetry, we set the inclined angle of the valley creases to be $\varphi_0 = \pi/3$, where it renders equilateral triangular facets in the tetrahedron hinges. We find that when $\varphi_0 \neq \pi/3$, folding of the hinges will lead to out-of-plane deformation in the hinged cut units (Appendix Fig. S1 A). In addition, when the cutting ratio m_t is small (e.g., $m_t < 0.5$ where the subscript "t" represents the case of triangular cuts), additional cutouts are needed to ensure compatible deformation (Appendix Fig. S1B), which will break the structural integrity. Thus, in this work, we limit our discussions to the cases of $\varphi_0 = \pi/3$ and $m_t > 0.5$ in the folded kirigami structures with triangular cuts and in-plane deformation of cut units.

3.2.1. Folding angle relation and folding rate

Fig. 4A-C show the schematics of projected shape changes in the folded kirigami structure with triangular cuts via hinge folding, where the mountain folding angle increases from 0 (Fig. 4A, non-folded) to π (Fig. 4C, completely folded). Fig. 4B shows a representative intermediate folded state. The rotation of a representative hexagonal cut unit enclosed by an equilateral triangle is highlighted in Fig. 4D-F. At the unfolded state, for the small equilateral triangle $T_{30}P_0P$ in Fig. 4D consisting of three lines of cuts, mountain creases, and valley creases, we set its side length l_1 to be $l_1 = (1-m_t)\,L_0$ and the length of $PP_4 = l_2$, where $L_0 = 2l_1 + l_2$ is the length of the enclosed large equilateral triangle $T_{10}T_{20}T_{30}$. After folding, the triangular $T_{10}T_{20}T_{30}$ transforms into a new equilateral triangle $T_1T_2T_3$ with side length of L (Fig. 4E(i)) and the three creases fold into a 3D tetrahedron hinge shown in Fig. 4E(ii). The opening angle between two cuts is defined as η_t (Fig. 4E(i)). From the geometry shown in Fig. 4E, we can obtain the following geometrical relationship between the side lengths as

$$\begin{aligned}
&N_1N = E_1N_1\tan\varphi_t = E_1E\tan\varphi_t/2,\ N_1E = \sqrt{3}EE_1/2\\
&P_0T_{30} = P_4T_{20} = E_1N = E_1N_1/\cos\varphi_t = EE_1/2\cos\varphi_t,\\
&T_3P_2 = PP_3/\tan\varphi_0 = l_2\sin(\eta_t/2)/\sqrt{3},\\
&P_2P_3 = P_1P = P_0P\sin\varphi_t/\sin\varphi_0 = 2\sqrt{3}l_1\sin\varphi_t/3,\\
&P_3P_4 = PP_4\cos(\eta_t/2) = l_2\cos(\eta_t/2)\\
&P_4T_2 = P_0P_1 + P_1T_3 = 2\sqrt{3}l_1\sin(2\pi/3-\varphi_t)/3\\
&\quad +2\sqrt{3}l_2\sin(\eta_t/2)/3\\
&T_3T_2 = T_3P_2 + P_2P_3 + P_3P_4 + P_4T_2\\
&= \left(\sqrt{3}\,(2m_t-1)\sin(\eta_t/2) + \cos(\eta_t/2)\right)L_0
\end{aligned} \tag{13}$$

where φ_t are the projected angle between the mountain and valley creases after folding with $\varphi_t = \pi/3 - \eta_t/2$.

The valley folding angle γ_v (i.e., the dihedral angle between the pop-up inclined plane $S_{EE_1E_3}$ and the base surface $S_{E_1E_2E_3}$) and mountain folding angle γ_m (i.e., the dihedral angle between surface $S_{EE_1E_3}$ and $S_{EE_1E_2}$, see Fig. 4E-ii) can be determined by $\cos\gamma_v = N_1N/N_1E$ and $\sin(\gamma_m/2) = N_2E_3/N_3E_3$ with $EN_1 \perp E_1E_2$ and $EN \perp S_{E_1E_2E_3}$. Thus, based on the geometrical conditions of $EE_1 = EE_3 = EE_2 = E_1E_3 = E_1E_2$ and Eq. (12), we have

$$\gamma_v = \arccos\left(\frac{\tan(\pi/3-\eta_t/2)}{\sqrt{3}}\right) \tag{14}$$

$$\gamma_m = \pi - 2\arcsin\left(\frac{2\sin(\pi/3-\eta_t/2)}{\sqrt{3}}\right) \tag{15}$$

Eqs. (14)–(15) show that it has a single degree of freedom η_t, which is the same as the case of square cuts. Note that despite the same tetrahedron hinge in both cases of folded kirigami structures with square and triangular cuts, their relationships between the folding angles and the opening angle of cuts are generally different considering their different rotational symmetries (i.e., four-fold symmetry in square cuts while three-fold symmetry in triangular cuts). We note that for the mountain folding angle γ_m, setting $\varphi_0 = \pi/3$ in Eq. (1) for the case of square cuts can reduce to Eq. (15), as seen from the same curve of $\gamma_m - \eta_s$ in Fig. 3A(i) (the olive dashed line with $\varphi_0 = \pi/3$) as that in Fig. 5A (the black line). However, it does not apply to the valley folding angle γ_v, i.e., Eq. (2) does not reduce to Eq. (14) at $\varphi_0 = \pi/3$, as evidenced by the distinct valley folding-opening angle curves in Fig. 3A(i) (convex curve, violet dashed line for square cuts) and Fig. 5A (concave curve, green line for triangular cuts).

Similarly, based on the geometrical relationship in Eqs. (14)–(15), the folding rate k_t can be obtained as

$$k_t = \tan\left(\arccos\left(\frac{\tan(\pi/3-\eta_t/2)}{\sqrt{3}}\right)\right) \tag{16}$$

Eq. (16) indicates that the folding rate is only dependent of the opening angle η_t ($0 < \eta_t < \pi/3$). For all designs with different cutting ratios m_t, as η_t approaches to $\pi/3$, Fig. 5B shows the similar J-shaped curve to the case of square cuts.

3.2.2. Nominal strains and surface porosity

With Eqs. (14)–(15), the nominal strains $(\varepsilon_{xx})_t$ and $(\varepsilon_{yy})_t$ for the folded kirigami structure with triangular cuts can be derived

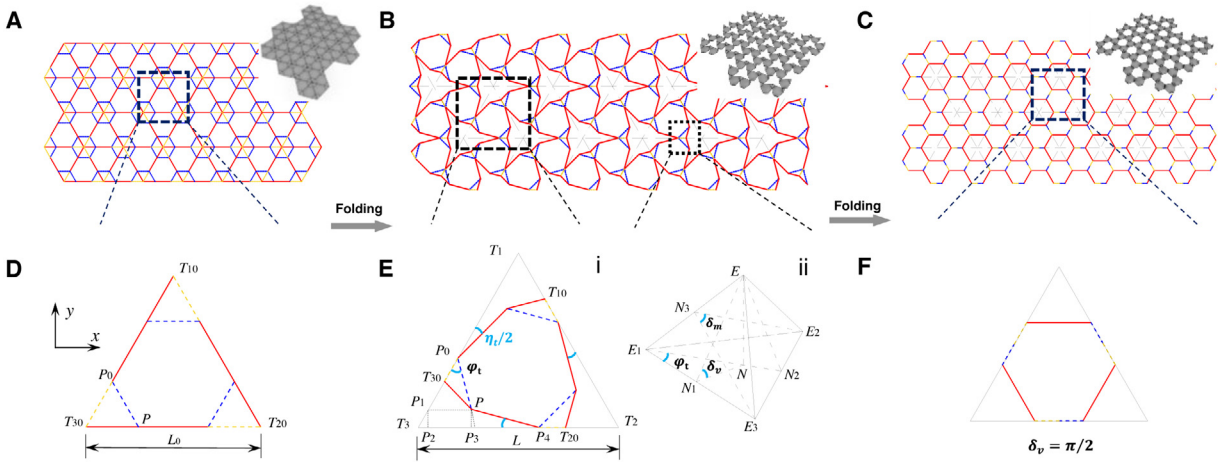

Fig. 4. Schematic of the projected view of shape changes in folded kirigami structures with triangular cuts. (A) non-folded state, (B) partially folded state, (C) completely folded state with the valley folding angle $\gamma_v = \pi/2$. Bottom row shows the schematics of the geometrical parameters in each folded state.

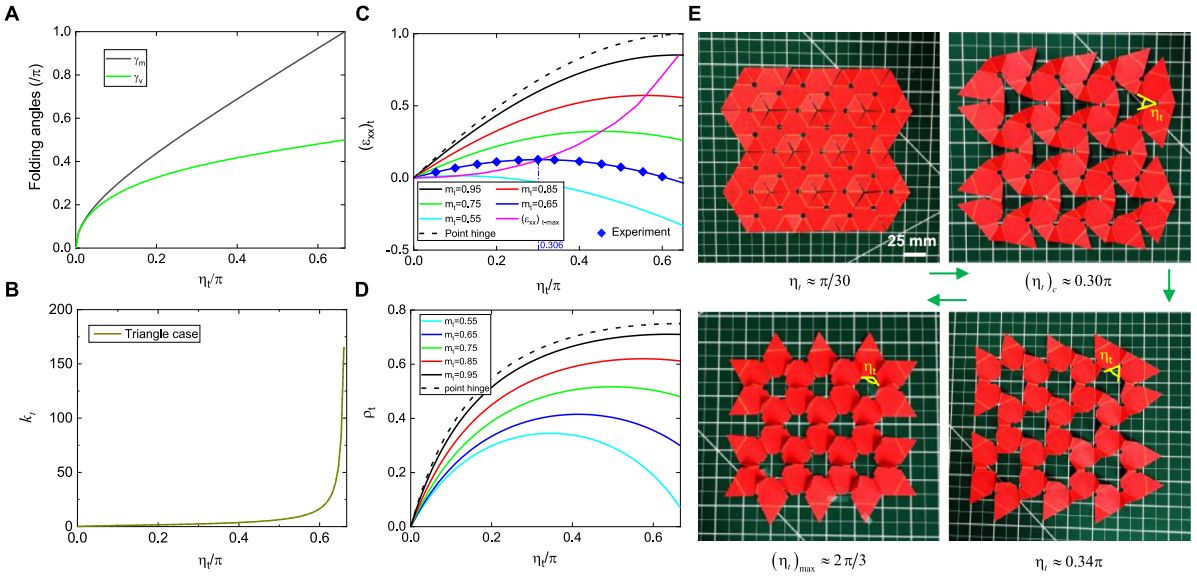

Fig. 5. Geometrical modeling of folded kirigami structures with triangle cuts ($\varphi_0 = \pi/3$). (A) Theoretical curves of mountain angle γ_m and valley angle γ_v vs. the opening angle η_t; (B) theoretical curve of folding rate k_s vs. η_t; (C) theoretical curves of nominal strain $(\varepsilon_{xx})_t$ vs. η_t for different cutting ratios m_t. Symbols represent the corresponding measured experimental data points; (D) theoretical curves of surface porosity ρ_t vs. η_t for different m_t. The dashed line in both (C) and (D) represents the case of kirigami sheets with point hinge when m_t approaches to 1. (E) Demonstrated shape changes in the paper-based folded krigiami structure prototype at representative values of η_t with $m_t = 0.65$. (For interpretation of the references to color in this figure legend, the reader is referred to the web version of this article.)

as

$$(\varepsilon_{xx})_t = (T_2T_3 - T_{20}T_{30})/T_{30}T_{20}$$
$$= \sqrt{3}(2m_t - 1)\sin(\eta_t/2) + \cos(\eta_t/2) - 1 \quad (17)$$
$$(\varepsilon_{yy})_t = \sqrt{3}(\varepsilon_{xx})_t/2$$

Eq. (17) also shows that it has a constant negative Poisson's ratio of $v_t = -\sqrt{3}/2$.

Similarly, the surface porosity ρ_t for the case of triangular cuts can be obtained as

$$\rho_t = 1 - \left(\sqrt{3}(1 - m_t)^2 \tan(\eta_t/2) - (3m_t - 1)^2 + 3(2m_t - 1)^2\right)\frac{L_0^2}{L^2} \quad (18)$$

Fig. 5C and D show the change of the nominal strain $(\varepsilon_{xx})_t$ and the surface porosity ρ_t with the opening angle η_t for the designs with different cut ratio m_t, respectively. Similar to the case of square cuts, for cut ratio $m_t \geq 0.55$, both $(\varepsilon_{xx})_t$ and ρ_t show a non-monotonic trend with a peak value, where they first increase and then decrease as η_t increases from 0 to $\pi/3$. This is consistent with the observed shape transition in the prototype with $m_t = 0.65$ shown in Fig. 5E. As η_t increases, it expands with an increasing ρ_t and achieves the peak strain with the maximally expanded shape at $(\eta_t)_c \approx 0.30\pi$ (top right of Fig. 5E), which agrees well with the theoretical prediction of $(\eta_t)_c = 0.306\pi$ in Fig. 5C. We note that the expanded shape with the peak strain does not corresponds to the peak porosity $(\rho_t)_{\max}$ that occurs at $\eta_t \approx 0.41\pi$ as seen from Fig. 5D. As η_t further increases, both $(\varepsilon_{xx})_t$ and ρ_t reduce until it becomes completely folded (bottom row of Fig. 5E). The corresponding measured nominal strains at different opening angles agree well with the theoretical prediction as shown in Fig. 5C.

As m_t increases, both the peak strain $(\varepsilon_{xx})_{t\text{-max}}$ (i.e., the purple curve in Fig. 5C) and peak porosity (Fig. 5D) increase and shift to

the right. Thus, at the extreme case of point-hinge without folds, i.e., $m_t = 1$, $(\varepsilon_{xx})_{t-\text{point-hinge}} = \sqrt{3}\sin(\eta_t/2) + \cos(\eta_t/2) - 1$ increases monotonically with η_t for $0 \le \eta_t \le \pi/3$ (Fig. 5C). At $(\eta_t)_c = \pi/3$, it shows the peak strain of 1 (Fig. 5C) and the peak porosity of 0.75 (Fig. 5D). By manipulating the cut ratio m_t, the nominal strain $(\varepsilon_{xx})_t$ can be largely tuned from – 0.35 ($m_t = 0.55$) to 0.95 ($m_t = 0.95$) with the corresponding porosity ρ_t changing from 0.05 to 0.7 (Fig. 5C-D). The tunable range of both strain and porosity is much wider than the case of square cuts with $(\varepsilon_{xx})_t$ ranging from – 0.35 ($m_s = 0.60$) to 0.386 ($m_s = 0.98$) and ρ_t ranging from 0 to 0.41 in Fig. 3A(v-vi).

3.3. Structural stiffness for the folded kirigami structures with square and triangular cuts

The above sections discuss the shape changes of the folded kirigami structures from the geometrical perspective. In this section, we theoretically analyze how the shape change affects their structural stiffness under uniaxial loads. We assume all line folds as linear elastic torsional spring with a constant stiffness k and all facets as rigid plates. For the folded kirigami structure under uniaxial loads, the potential elastic energy Π is

$$\Pi = \mathrm{U} - \mathrm{W} \tag{19}$$

where U is the stored elastic energy and $\mathrm{W}=\int_{\gamma_{m0}}^{\gamma_m} F(dl/d\gamma_m')d\gamma_m'$ is the work done by the external force F, where l is the length of the unit cell. Considering its periodicity, we select one unit cell to conduct structural stiffness analysis for both square and triangular cuts.

Square cuts: For the case of square cuts, from Fig. 2A, we can determine its elastic energy density U_s as

$$\mathrm{U}_s = 4kl_m(\gamma_m - \gamma_{m0})^2 + 8kl_v(\gamma_v - \gamma_{v0})^2 \tag{20}$$

where l_m and l_v are the length of mountain and valley creases, respectively; γ_{v0} and γ_{m0} are the valley and mountain folding angles at a certain deformed state, respectively, which satisfy the relationship in Eq. (2), i.e.,

$$\gamma_{v0} = \arcsin\frac{\cos(\gamma_{m0}/2)}{\sqrt{\sin^2\varphi_0\cos^2(\gamma_{m0}/2) + \cos^2\varphi_0}} \tag{21}$$

For a randomly selected deformed state, the condition for the external force being in equilibrium should satisfy that the first variation of potential energy Π with respect to γ_m equals to zero, i.e.,

$$\delta\Pi/\delta\gamma_m = 0 \tag{22}$$

Thus, by combining Eqs. (1), (2), (5)–(6), and Eqs. (20)–(22), we can derive the explicit form for external force F as

$$F = \frac{dU_s/d\gamma_m}{da/d\gamma_m} = 8kl_m(\gamma_m - \gamma_{m0})M_1 + 16kl_v(\gamma_v - \gamma_{v0})M_2 \tag{23}$$

where M_1 and M_2 are

$$M_1 = \left(\frac{da}{d\gamma_m}\right)^{-1} = \left\{\cos(\gamma_m/2)\left(4\sin^2\varphi_0 - \sin^2\varphi_0\right) - \frac{\sin\gamma_m\sin^2\varphi_0(\cos\varphi_0 + \sin\varphi_0)}{4\sqrt{1-\sin^2(\gamma_m/2)\sin^2\varphi_0}}\right\}^{-1}$$

$$M_2 = \frac{d\gamma_v/d\gamma_m}{da/d\gamma_m} = \cos(\gamma_m/2)\tan\varphi_0 \times \left\{\frac{\left(1-\sin^2(\gamma_m/2)\sin^2\varphi_0\right)(\cos\varphi_0 - 2\sin\varphi_0) + }{\sin(\gamma_m/2)(\sin 2\varphi_0 + \sin 2\varphi_0)\sqrt{1-\sin^2(\gamma_m/2)\sin^2\varphi_0}}\right\} \tag{24}$$

Then, based on Eq. (23), we can finally determine the structural stiffness of the square cut case under uniaxial loads F by [37]

$$K_s(\varphi_0, \gamma_{m0}) = dF/d\gamma_m\big|_{\gamma_{m0}} \tag{25}$$

Triangular cuts: For the case of triangle cuts, given its three-fold structural symmetry, we explore its structural stiffness by aligning the uniaxial loads along one of the principal axes. Here, based on the built Cartesian coordinate systems in Fig. 4A, we select y-axis as the external force direction. Thus, from Fig. 4A, we can determine the elastic energy density for a unit as

$$\mathrm{U}_t = 1.5kl_2(\gamma_m - \lambda_{m0})^2 + 3kl_2(\gamma_v - \gamma_{v0})^2 \tag{26}$$

where $l_2 = (2m_t - 1)L_0$, and the folding angles γ_{v0} and γ_{m0} at a certain deformed state that satisfy Eqs. (14)–(15) are

$$\gamma_{m0} = \pi - 2\arcsin\left(2\sqrt{3}\sin(\pi/3 - \eta_{t0}/2)/3\right), \quad \gamma_{v0} = \arccos\left(\tan(\pi/3 - \eta_{t0}/2)/\sqrt{3}\right) \tag{27}$$

where η_{t0} is the corresponding opening angle.

Then, according to Eq. (22), the external force F^* can be derived as

$$F^* = \frac{dU_t/d\gamma_m}{dL/d\gamma_m} = \frac{dU_t/d\eta_t}{dL/d\eta_t} = \frac{3kl_2[(\gamma_m - \gamma_{m0})N_1 + 2(\gamma_v - \gamma_{v0})N_2]}{L_0\left[\sin(\eta_{t0}/2) - \sqrt{3}(1-2m_t)\cos(\eta_{t0}/2)\right]} \tag{28}$$

where $N_1 = d\gamma_m/d\eta_t$ and $N_2 = d\gamma_v/d\eta_t$ can be derived from Eqs. (14)–(15).

Thus, based on Eqs. (13)–(15) and (26)–(28), the structural stiffness K_t for triangular cuts under uniaxial loads can be determined by

$$K_t(m_t, \varphi_t) = dF^*/d\gamma_m\big|_{\gamma_{m0}} = dF^*/d\eta_t\big|_{\eta_{t0}} \tag{29}$$

Then, in principle, the stiffness along any other direction could be readily determined by their transformation matrices relative to the principal direction. Given the complex forms of Eqs. (25) and (29), we numerically solve them using the software MATLAB. The numerical results are presented in Fig. 6.

For the case of square cuts, Fig. 6A plots the variations of its normalized elastic energy density $\overline{U}_s = U_s/ka_0^2$ with respect to the opening angle η_s for the designs with different inclined angle φ_0 at $m_s = 0.75$, where $0 \le \eta_s \le \varphi_0$ for each given φ_0. It shows that $\overline{U}_s$ increases monotonically with the opening angle for all φ_0. As φ_0 increases, the maximum elastic energy density $(\overline{U}_s)_{\max}$ (dashed line) at the maximum opening angle $(\eta_s)_{\max} = \varphi_0$ also increases due to the increased length of valley creases. Fig. 6B shows the corresponding numerical results on the normalized structural stiffness $\overline{K}_s = K_s/k$ as a function of η_s at $m_s = 0.75$. At $\eta_s = 0$, it shows a structural singularity with an infinite stiffness for all different values of φ_0. As the line cuts start to open with a small opening angle of 0.01π, the stiffness drops dramatically to 0.2×10^2 due to the stretching-induced pop-up of hinges via folding. The inset figure with the zoom-in view of the stiffness curves shows that the folded kirigami structures with a smaller inclined angle φ_0 generally possess a relatively higher structural stiffness. Thus, the folded kirigami structures with a larger φ_0 are easier to open upon uni-axial loading. As η_s further increases, it encounters another structural singularity point at the same opening angle for all different values of φ_0. Beyond the singularity point, the stiffness becomes negative and increases with further opening. By comparing the positions of the opening angle for the singular stiffness in Fig. 6B and the peak nominal strains in Fig. 3B(v) ($m_s = 0.75$), we find that both angles

give the identical critical value of $(\eta_s)_c = 0.296\pi$, indicating that the point of polarization switch at the maximally stretched state corresponds to an infinite structural stiffness. Beyond the singular stiffness point, the structure starts to shrink under uniaxial loading, which leads to a negative stiffness as observed in Fig. 6B.

Similarly, for folded triangular cut kirigami structures with different cut length ratios m_t, we plot the numerical results of both normalized elastic energy density $\overline{U}_t = U_t/kL_0^2$ and normalized structural stiffness $\overline{K}_t = K_t/k$ *vs.* the opening angle η_t, where $\varphi_0 = \pi/3$ is kept the same. Fig. 6C shows that the elastic energy density $\overline{U}_t$ decreases with the increasing value of m_t, which is reasonable due to the higher folding energy in the folded structures with smaller cut lengths (i.e., larger crease length). As m_t increases from 0.55 to 0.95, the maximum elastic energy density $(\overline{U}_t)_{\max}$ at the maximum opening angle $(\eta_t)_{\max} = \pi/3$ decreases by 10 folds (the dashed line in Fig. 6C). Similar to the case of square cuts, the structural stiffness for triangular cuts in Fig. 6D shows two singular points, one is at the onset of cut opening (i.e., $\eta_t = 0$), the result of which is not shown for clarity, and the other is at the critical opening angle that corresponds to the maximum nominal strains for each given m_t. We have the identical $(\eta_s)_c = 0.23\pi$, 0.28π, and 0.33π, i.e., the polarization switch point, for the onsets of both singular stiffness in Fig. 6D and peak strains in Fig. 5C for $m_t = 0.75$, 0.85, and 0.95, respectively. Thus, a larger m_t could delay the occurrence of polarization switch. Meanwhile, the inset figure on the zoom-on view of the stiffness shows that the structural stiffness decreases with the increasing m_t due to the reducing folding hinge sizes.

By comparing the zoom-in stiffness curves in the insets of Fig. 6B and D, we note that for both folded square-cut and triangular-cut kirigami structures with the same cutting ratio (e.g., $m_s = m_t = 0.75$), the triangular cut structure exhibits a higher structural stiffness than that of square cuts when evaluated at the same opening angle. For example, at $\eta_s = \eta_t = 0.2\pi$, $\overline{K}_t \approx 70$ for the triangular cut, which is over twice higher than that of the square cuts with $\overline{K}_s \approx 29.5$.

4. Tunable bandgaps of the folded kirigami structures

Square cuts: The shape change in the folded kirigami structures makes it possible to tune their potential phononic band structures through the opening and closing of pores. Since the band structures are mainly determined by the deformed configurations in the square cuts characterized by the opening angle η_s, next, we numerically explore the evolution of the bandgaps with the changing η_s in the folded kirigami structures using finite element simulation. Specially, the designs with different parameters of inclined angle φ_0 and the cutting ratio m_s in the periodic unit cells are studied.

The finite element analysis is performed on the two-dimensional projection of the selected unit under different opening angles through the acoustics module in COMSOL. For the bandgap structure analysis, eigenfrequency study is simulated for an infinite structure by defining a single unit cell with periodic Block–Floquet boundary conditions, shown as in the insets of Fig. 7A(ii)- C(ii). In the simulation, the first twenty eigenfrequencies ω are calculated and normalized as $\overline{\omega} = \omega A_0/2\pi C_T$, where A_0 is the undeformed unit cell length, and $C_T = \sqrt{\mu/p}$ is the transverse plane wave velocity with $C_T = 170.25$ m/s for assumed PET materials with shear modulus $\mu = 40$ MPa and density $\rho = 1380$ kg/m^3. The simulation is repeated with a 5° incremental opening angle and the obtained normalized frequencies are plotted correspondingly. For the transmission loss analysis, as shown in Fig. 7D, we construct a 5 × 5 periodic structure whose ends are coupled with two rectangular air domains with perfectly matched layers. The left domain (labeled as B in Fig. 7D) is specified as the background pressure field with 1 Pa sound pressure. The transmission loss is defined as the difference of the averaged sound pressure between the left and right boundaries of the layered structure. Finally, the sound pressure level is plotted by arraying the 5 × 5 periodic structure vertically.

Fig. 7A(i)-C(i) show the comparison of bandgap diagrams as a function of the opening angle η_s (equivalently the nominal strain ε) between three representative periodic unit cells, where $\varphi_0 = 45°$ and $m_s = 0.8$ in Fig. 7A, $\varphi_0 = 45°$ and $m_s = \sqrt{2}/2$ in Fig. 7B, and $\varphi_0 = 70°$ and $m_s = 0.8$ in Fig. 7C, respectively. Specially, the sub-unit in Fig. 7B takes a regular octagonal shape. The blue curves show the corresponding nominal strain ε as a function of η_s in terms of Eq. (9). Within the studied eigenfrequency range, Fig. 7A(i)-C(i) show that all the three structures exhibit a similar distribution of four combined bandgaps, either wide continuous (bandgap I and IV) or discrete (bandgap II and III), evolving with the increase of η_s. The dispersion curves for the specified opening angles with peak nominal strains are shown in Fig. 7A(ii)-C(ii). The bandgaps are denoted by the shaded area that prohibit acoustic waves from traveling through within the corresponding frequency range. The maximum transmission loss in both bandgap I and IV at the peak strain is more than 200 dB for all the three structures (Fig. 7A-C, iii). In bandgap I of all the three structures, there exists an abrupt increase of the transmission at around normalized frequency 0.3, which can be explained by the overall size effect. Fig. 7D shows an example of the sound pressure distribution in an assembly of 5 × 5 unit cells ($\varphi_0 = 70°$, $m_s = 0.8$), where the sound transmission is forbidden at the bandgap frequencies with significantly different sound pressure level on the two sides of the structure, while the sound transmission beyond the bandgap range is allowed.

Interestingly, Fig. 7B(i) shows that the unit cell ($\varphi_0 = 45°$ and $m_s = \sqrt{2}/2$) exhibits a symmetric bandgap diagram about the axis of $\eta_s = 45°$ with the peak strain. As η_s increases, the structure undergoes a polarization switch and ε becomes zero at its maximum opening angle of 90°. We believe that such a symmetric band structure is attributed to the rotational symmetry of regular octagon shape in the sub-unit and the related structure polarization switch. Similar polarization switch is also observed for the unit cell with a larger $\varphi_0 = 70°$ in Fig. 7C(i). However, it shows an asymmetric band structure about the axis of $\eta_s = 60°$ at the peak strain. In addition, rather than an open pore shape at $\eta_s = 90°$ in Fig. 7B(i), the pore transits to be nearly closed and ε becomes negative at its maximum opening angle of 140°. We note that the polarization switch in both structures leads to a narrow necking and discontinuity in the bandgap II of the diagram in Fig. 7B(i) and C(i), which occurs around the position with the peak strain, also the transition point for the onset of polarization switch.

Indeed, different bandgap structures can not only be achieved by choosing different inclined angle φ_0 and cutting ratio m_s, but also be tuned by changing the opening angle for a specific design. For example, for the kirigami structure shown in Fig. 7A(i), as the opening angle increases from 0° to 90°, the bandwidth of bandgap I can be tuned from the narrowest at the opening angle $\eta_s \approx 30°$ with $\overline{\omega} \in [0.16, 0.38]$ to the widest at $\eta_s = 90°$ with $\overline{\omega} \in [0.02, 0.58]$. Bandgap III is the most tunable, where it shows no bandgap at $\eta_s \approx 45°$ but a large bandwidth with $\overline{\omega} \in [0.43, 0.85]$ at $\eta_s \approx 0°$. Overall, for all the three kirigami structures in Fig. 7A(i)-C(i), bandgaps II, III and IV show a narrower bandwidth distribution but relatively higher tenability, while bandgap I has a wider bandwidth but limited tunability in terms of opening new bandgaps.

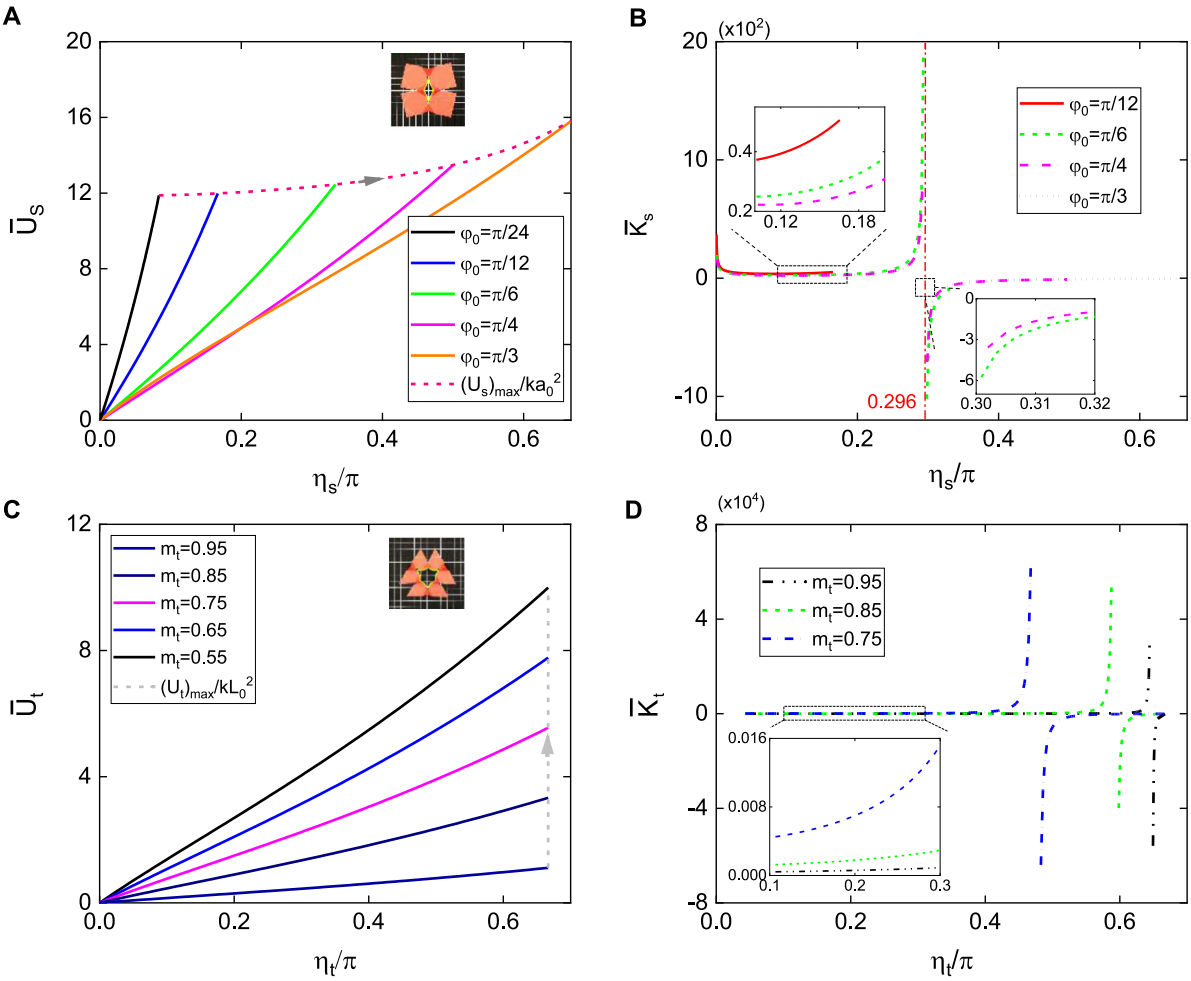

Fig. 6. Structural stiffness analysis of folded kirigami structures with square and triangle cuts. (A) Predicted curves of normalized elastic spring torsional energy stored in folds $\overline{U}_s$ ($= U_s/ka_0^2$) vs. the opening angle η_s for square cut designs with different inclined angles φ_0 at fixed cutting ratio $m_s = 0.75$. The dashed line represents the maximum normalized $\overline{U}_s$ for different φ_0; (B) The corresponding predicted curves of normalized structural stiffness $\overline{K}_s$ ($= K_s/k$) vs. η_s for designs in (A). Inset shows the zoom-in view of the curves. (C) Predicted curves of normalized elastic spring torsional energy stored in folds $\overline{U}_t$ ($= U_t/kL_0^2$) vs. the opening angle η_t for triangular cut designs with different cutting ratio m_t at fixed inclined angle $\varphi_0 = \pi/3$. The dashed line represents the maximum normalized $\overline{U}_t$ for different m_t; (D) The corresponding predicted curves of normalized structural stiffness $\overline{K}_t$ ($= K_t/k$) vs. η_t for designs in (C). Inset shows the zoom-in view of the curves.

Triangular cuts: Based on the results of tunable bandgaps from the shape changes in the case of square cuts, here, we focus on how the unit shape (i.e., the triangular cuts) affects the band structure. We choose a representative structure with $m_t = 0.8$ and $\varphi_0 = 60°$ for comparison.

Fig. 8A shows the calculated band structure evolution with the opening angle η_t as it increases from 0° to 120°. The blue curve shows the corresponding nominal strain calculated from Eq. (17). Similarly, the band structures show both wide continuous and discrete bandgap evolution with the strain. Compared to the similar case of square cuts in Fig. 7C, it exhibits a more complex band structure in terms of the bandgap distribution and opening/closing of new bandgaps shown in Fig. 8A. Fig. 8B shows the specified band structure at the peak strain. It shows more bandgaps but narrower bandwidths than that for square cuts in Fig. 7C(ii). For example, the triangular cut shows 9 distributed narrow bandgaps ranging from normalized frequency of 0.08 to 0.9 (Fig. 8C), while the square case shows 4 wide bandgaps ranging from normalized frequency of 0.19 to 0.9 (Fig. 7C(ii)). In addition, the transmission losses shown in Fig. 8C in the range of bandgap frequency are more significant, whose maximum can be more than 50 dB in several wide bandgaps.

We note that both the square cuts and the triangular cuts show higher bandgap tunability than the reported conventional kirigami structures with point-like hinges [10] Given the similar overall geometric shape and porosity in both kirigami structures with and without folding hinges, the conventional kirigami structure with square cuts shows a distribution of multiple parallel bandgaps at different frequencies [10]. In addition, the bandwidths of all the parallel bandgaps remain almost unchanged with the applied strain until the strain exceeds 15% [10]. In comparison, the square cuts in Fig. 7A(i)-C(i) and the triangular cuts in Fig. 8A with foldable hinges show more complex bandgaps with curved boundaries, enabling a much higher bandgap tunability.

5. Conclusions

In summary, through combined modeling and experiments, we explore quantifying the effects of 3D folding hinges on the shape changes of a new class of folded kirigami structures as well as the shape determined structural stiffness and band structure evolution. Compared to the conventional non-folded kirigami structures with point hinges, the folded kirigami structure introduces several newly added folding-related parameters that lead to distinct shape-changing behaviors. The folding hinge design enables the potential unique polarization switch that is

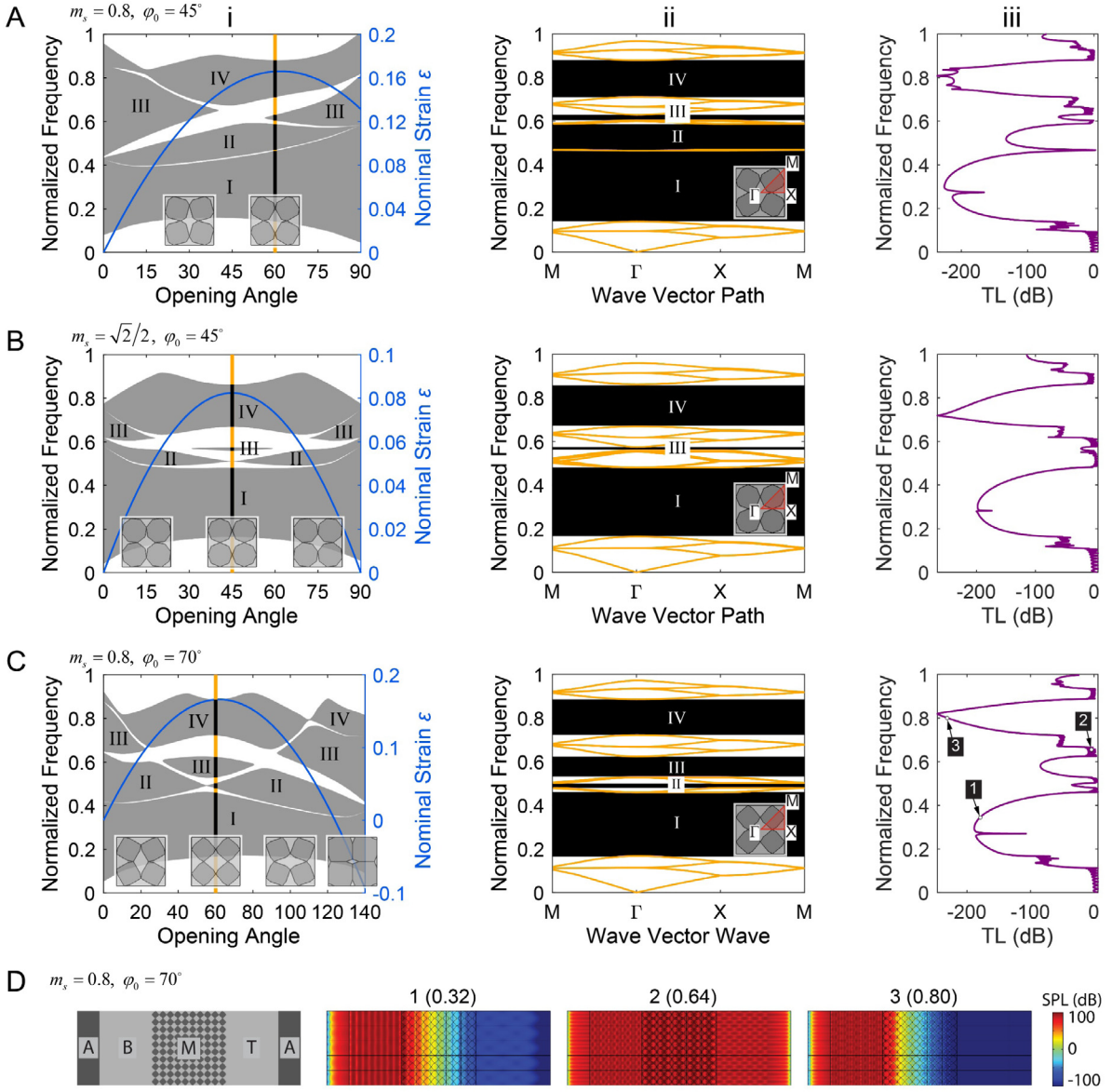

Fig. 7. Tunable band structures of folded kirigami structures with square cuts. (A-C) column (i): the evolution of bandgap structures with the opening angle and the corresponding nominal strain for three representative kirigami structures with inclined angle $\varphi_0 = 45^\circ$ and cutting ratio $m_s = 0.8$ in (A), $\varphi_0 = 45^\circ$ and $m_s = \sqrt{2}/2$ in (B), and $\varphi_0 = 70^\circ$ and $m_s = 0.8$ in (C); column (ii) and column (iii): The corresponding bandgap structures and transmission loss at the opening angle with the maximum nominal strain, respectively. (D) Sound pressure distribution in an assembly of 5 by 5 unit cells ($\varphi_0 = 70^\circ$ and $m_s = 0.8$). (For interpretation of the references to color in this figure legend, the reader is referred to the web version of this article.)

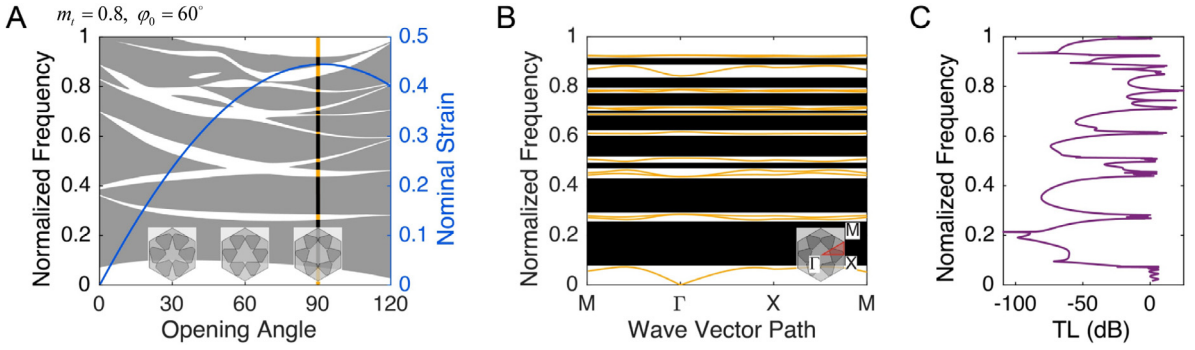

Fig. 8. Tunable band structures of folded kirigami structures with triangular cuts (cutting ratio $m_t = 0.8$ and inclined angle $\varphi_0 = 60^\circ$). (A) The evolution of bandgap structures with the opening angle and the corresponding nominal strain. (B-C) The corresponding bandgap structure (B) and transmission loss (C) at the peak strain with opening angle of 90°.. (For interpretation of the references to color in this figure legend, the reader is referred to the web version of this article.)

not observed in its non-folded counterpart. A geometric model is developed to predict the effects of the prescribed governing geometrical parameters such as the inclined angles and the cutting ratio on the shape changes of the folded kirigami structures, including the folding angle, nominal strains, folding rate, and surface porosity. The model is validated through related experiments. The geometrical design space for the occurrence of polarization switch is identified. Moreover, a geometric mechanics model is developed to quantify the shape changes on the structural stiffness. Lastly, its potential application in achieving tunable bandgaps in the folded kirigami structures is explored through numerical simulation by manipulating the cutting ratio and the inclined crease angle.

The current study mainly focuses on the in-plane deformation of the folded kirigami sheets. We note that the folding hinge design can also enable the out-of-plane deformation as demonstrated in Fig. S1B in the Appendix. How the geometry of the folding hinges affects the rich out-of-plane deformation in different folded kirigami sheets will be left for future studies. We believe that the folded kirigami design could also be applicable to thick kirigami structures, as well as self-folding shape-morphing machines and soft robots.

Declaration of competing interest

The authors declare that they have no known competing financial interests or personal relationships that could have appeared to influence the work reported in this paper.

Acknowledgments

J. Y. acknowledges the funding support from National Science Foundation (CMMI-CAREER-2005374), USA. H. L. acknowledges the funding support from National Science Foundation (CMMI-1663135), USA.

Appendix A. Supplementary data

Supplementary material related to this article can be found online at https://doi.org/10.1016/j.eml.2021.101483.

References

[1] D.M. Sussman, Y. Cho, T. Castle, X. Gong, E. Jung, S. Yang, et al., Algorithmic lattice kirigami: A route to pluripotent materials, Proc. Natl. Acad. Sci. 112 (24) (2015) 7449–7453.
[2] T. Castle, D.M. Sussman, M. Tanis, R.D. Kamien, Additive lattice kirigami, Sci. Adv. 2 (9) (2016) e1601258.
[3] R.M. Neville, F. Scarpa, A. Pirrera, Shape morphing kirigami mechanical metamaterials, Sci. Rep. 6 (1) (2016) 31067.
[4] Q. Zhang, J. Wommer, C. O'Rourke, J. Teitelman, Y. Tang, J. Robison, et al., Origami and kirigami inspired self-folding for programming three-dimensional shape shifting of polymer sheets with light, Extreme Mech. Lett. 11 (2017) 111–120.
[5] S.J.P. Callens, A.A. Zadpoor, From flat sheets to curved geometries: Origami and kirigami approaches, Mater. Today 21 (3) (2018) 241–264.
[6] X. Ning, X. Wang, Y. Zhang, X. Yu, D. Choi, N. Zheng, et al., Assembly of advanced materials into 3D functional structures by methods inspired by origami and kirigami: A review, Adv. Mater. Interfaces 5 (13) (2018) 1800284.
[7] J. Cui, F.R. Poblete, Y. Zhu, Origami/kirigami-guided morphing of composite sheets, Adv. Funct. Mater. 28 (44) (2018) 1802768.
[8] J.N. Grima, K.E. Evans, Auxetic behavior from rotating squares, J. Mater. Sci. Lett. 19 (17) (2000) 1563–1565.
[9] Y. Cho, J.-H. Shin, A. Costa, T.A. Kim, V. Kunin, J. Li, et al., Engineering the shape and structure of materials by fractal cut, Proc. Natl. Acad. Sci. 111 (49) (2014) 17390–17395.
[10] Y. Tang, G. Lin, L. Han, S. Qiu, S. Yang, J. Yin, Design of hierarchically cut hinges for highly stretchable and reconfigurable metamaterials with enhanced strength, Adv. Mater. 27 (44) (2015) 7181–7190.
[11] Y. Tang, J. Yin, Design of cut unit geometry in hierarchical kirigami-based auxetic metamaterials for high stretchability and compressibility, Extreme Mech. Lett. 12 (2017) 77–85.
[12] Y. Zhang, Z. Yan, K. Nan, D. Xiao, Y. Liu, H. Luan, et al., A mechanically driven form of kirigami as a route to 3D mesostructures in micro/nanomembranes, Proc. Natl. Acad. Sci. 112 (38) (2015) 11757–11764.
[13] M.K. Blees, A.W. Barnard, P.A. Rose, S.P. Roberts, K.L. McGill, P.Y. Huang, et al., Graphene kirigami, Nature 524 (7564) (2015) 204–207.
[14] A. Rafsanjani, K. Bertoldi, Buckling-induced kirigami, Phys. Rev. Lett. 118 (2017) 084301.
[15] G.P.T. Choi, L.H. Dudte, L. Mahadevan, Programming shape using kirigami tessellations, Nature Mater. 18 (9) (2019) 999–1004.
[16] T.C. Shyu, P.F. Damasceno, P.M. Dodd, A. Lamoureux, L. Xu, M. Shlian, et al., A kirigami approach to engineering elasticity in nanocomposites through patterned defects, Nature Mater. 14 (8) (2015) 785–789.
[17] M. Isobe, K. Okumura, Initial rigid response and softening transition of highly stretchable kirigami sheet materials, Sci. Rep. 6 (1) (2016) 24758.
[18] S. Shan, S.H. Kang, Z. Zhao, L. Fang, K. Bertoldi, Design of planar isotropic negative Poisson's ratio structures, Extreme Mech. Lett. 4 (2015) 96–102.
[19] N. An, A.G. Domel, J. Zhou, A. Rafsanjani, K. Bertoldi, Programmable hierarchical kirigami, Adv. Funct. Mater. 30 (6) (2020) 1906711.
[20] Y. Tang, G. Lin, S. Yang, Y.K. Yi, R.D. Kamien, J. Yin, Programmable kiri-kirigami metamaterials, Adv. Mater. 29 (10) (2017) 1604262.
[21] D.-G. Hwang, M.D. Bartlett, Tunable mechanical metamaterials through hybrid kirigami structures, Sci. Rep. 8 (1) (2018) 3378.
[22] Y. Yang, M.A. Dias, D.P. Holmes, Multistable kirigami for tunable architected materials, Phys. Rev. Mater. 2 (11) (2018) 110601.
[23] Y. Li, Q. Zhang, Y. Hong, J. Yin, 3D Transformable modular kirigami based programmable metamaterials, Adv. Funct. Mater. (2021) 2105641.
[24] Z. Song, X. Wang, C. Lv, Y. An, M. Liang, T. Ma, et al., Kirigami-based stretchable lithium-ion batteries, Sci. Rep. 5 (1) (2015) 10988.
[25] Y.-S. Guan, Z. Zhang, Y. Tang, J. Yin, S. Ren, Kirigami-inspired nanoconfined polymer conducting nanosheets with 2000% stretchability, Adv. Mater. 30 (20) (2018) 1706390.
[26] Y. Morikawa, S. Yamagiwa, H. Sawahata, R. Numano, K. Koida, M. Ishida, et al., Ultrastretchable kirigami bioprobes, Adv. Healthc. Mater. 7 (3) (2018) 1701100.
[27] K. Xu, Y. Lu, S. Honda, T. Arie, S. Akita, K. Takei, Highly stable kirigami-structured stretchable strain sensors for perdurable wearable electronics, J. Mater. Chem. C 7 (31) (2019) 9609–9617.
[28] A. Rafsanjani, Y. Zhang, B. Liu, S.M. Rubinstein, K. Bertoldi, Kirigami skins make a simple soft actuator crawl, Science Robotics 3 (2018) eaar7555.
[29] Y. Tang, Y. Li, Y. Hong, S. Yang, J. Yin, Programmable active kirigami metasheets with more freedom of actuation, Proc. Natl. Acad. Sci. 116 (52) (2019) 26407–26413.
[30] Y.-C. Cheng, H.-C. Lu, X. Lee, H. Zeng, A. Priimagi, Kirigami-based light-induced shape-morphing and locomotion, Adv. Mater. 32 (7) (2020) 1906233.
[31] Y. Yang, K. Vella, D.P. Holmes, Grasping with kirigami shells, Science Robotics 6 (54) (2021) eabd6426.
[32] V. Kunin, S. Yang, Y. Cho, P. Deymier, D.J. Srolovitz, Static and dynamic elastic properties of fractal-cut materials, Extreme Mech. Lett. 6 (2016) 103–114.
[33] A. Lamoureux, K. Lee, M. Shlian, S.R. Forrest, M. Shtein, Dynamic kirigami structures for integrated solar tracking, Nature Commun. 6 (1) (2015) 8092.
[34] L. Fang, J. Li, Z. Zhu, S. Orrego, S.H. Kang, Piezoelectric polymer thin films with architected cuts, J. Mater. Res. 33 (3) (2018) 330–342.
[35] S. Ming, C. Zhou, T. Li, Z. Song, B. Wang, Energy absorption of thin-walled square tubes designed by kirigami approach, Int. J. Mech. Sci. 157–158 (2019) 150–164.
[36] S. Yang, I.-S. Choi, R.D. Kamien, Foldable materials via fractal cuts and lattice kirigami, MRS Bull. 41 (2) (2016) 130–138.
[37] Z.Y. Wei, Z.V. Guo, L. Dudte, H.Y. Liang, L. Mahadevan, Geometric mechanics of periodic pleated origami, Phys. Rev. Lett. 110 (21) (2013) 215501.